Chapter 3

In-situ TEM Study of Dislocation-Interface Interactions

Nan Li and Jian Wang

Additional information is available at the end of the chapter

http://dx.doi.org/10.5772/60880

Abstract

In this chapter, we highlighted the in situ transmission electron microscope (TEM) observation of the interactions of dislocations with three types of interfaces: (i) twin boundaries in Cu; (ii) metallic interphase boundaries; and (iii) metal/ceramic interfaces. Interface structures, interface properties, and dislocation-interface interactions are characterized in a high-resolution TEM. These knowledge provided insights into the understanding of the physical properties of materials, developing materials modeling tools incorporating interface deformation physics, and designing materials with desired properties.

Keywords: Interfaces, dislocations, multilayers, TEM

1. Introduction

Extensive investigations over the past decade indicate that nanolayered composites have unprecedented levels of strength, ductility, and damage tolerance in extreme environments [1-10]. As the length-scale is reduced from micro- to nano-scales, interfaces become crucial in determining mechanical properties of nano-scale materials due to the change of deformation mechanisms from phase-dominated to interface-dominated [10]. Atomic-scale modeling is able to reveal unit processes (involving single or a few defects) occurring at interfaces during deformation with respect to kinetics and energetics, but is limited to time-scale (ns) and length-scale (nm) [11-21]. Current state-of-the-art micro-scale, meso-scale, and continuum scale modeling works well for micro-scale materials because of the dominated deformation processes by dislocation activities in phases. Due to the less dependence of deformation on interfaces, interfaces often are phenomenologically treated as boundaries without any

structural characteristics [22-28]. For materials containing the high density of interfaces, it is still a challenge in incorporating interface physics, such as nucleation, motion, reactions, etc., in current models [29]. One of the bottlenecks is ascribed to the lack knowledge of interface-dominated deformation mechanisms because of the complexity of dislocation-interface interactions. To correlate the characteristics of interface with mechanical properties and behavior related to interfaces, it is essential to understand interfacial structure-property relationships at different scales and develop new materials modeling tools that incorporate interface physics and are able to address interface roles in terms of dislocation activity during mechanical deformation. Characterization of microstructures, defects, and defects interactions using ex situ and in situ microscopies has provided insights into understanding physical properties of materials, developing materials modeling tools incorporating interface deformation physics, and designing materials with desired properties [29].

In this chapter, we highlighted the in situ TEM observation of the interactions of dislocations with three types of interfaces: (i) twin boundaries in Cu; (ii) metallic interphase boundaries; and (iii) metal/ceramic interfaces. In situ nanoindentation tests were performed at room temperature in a Tecnai G(2) F30 microscope with a Nanofactory transmission electron microscopy-scanning tunneling microscopy (TEM-STM) platform. A Gatan CCD camera was used to capture the deformation of specimen during indentation with 3 frames/sec. The indenter tip made of W with a radius of 20 ~ 100 nm was pushed into the sample.

2. Twin boundaries in Cu

Metals with nanotwinned structure have received extremely high attention recently due to their unusual combination of properties of ultrahigh strength, high ductility, and high thermal stability, while still retaining the high electrical conductivity [30-42]. Twin boundaries surrounding a twin consist of coherent twin boundary and Σ3{112} incoherent twin boundaries (ITBs). Corresponding to crystallography of twins, the twinned and the matrix crystals have mirror symmetry across coherent twin boundary (CTB), causing the discontinuity of slip systems across CTBs. Thus, coherent twin boundaries can act as strong barriers for dislocation transmission, as demonstrated by both experiments and molecular dynamics (MD) simulations [41-47]. MD simulations have been used to explore the possible mechanisms for the transmission of a dislocation across a CTB with respect to the incoming dislocations and the stress states [48-54]. Using in situ TEM, ITBs have been observed to exert a crucial role over the mechanical deformation [55-61]. In this section, we characterized dislocation structure of Σ3{112} ITB in nanotwinned Cu, and investigated dislocation—CTB/ITB interactions using in situ TEM technique. Nanotwinned Cu is synthesized through physical vapor deposition on a 10% HF-etched Si (110) substrate at room temperature [34]. The chamber was evacuated to a base pressure of $\leq 5 \times 10^{-8}$ torr prior to deposition. The deposition rate was varied in the range of 0.6-4.0 nm s^{-1}.

2.1. Dislocation structure of Σ3 {112} ITB

Dislocation structure of Σ3{112} ITB was characterized according to the cross-sectional, high-resolution transmission electron microscope (HRTEM) image and dislocation theory. Figure

http://dx.doi.org/10.5772/60880

1a shows twin boundaries Σ3 {111} CTB oriented normal to the growth direction and Σ3 {112} ITB parallel to the growth direction. Along the Σ3 {112} ITB we observed a repeatable pattern with a unit involving three {111} atomic planes. Corresponding to crystallography of Σ3 twin, we constructed a schematic pattern of Σ3 {112} ITB as shown in Figure 1b. The {111} planes in the matrix crystal and in the twined crystal have a stacking sequence...ABCABC... and...ACBACB..., respectively. It is noticed that the stacking changing can be accomplished by the glide of any of the three Shockley partial dislocations, $\mathbf{b}_1$, $\mathbf{b}_2$, $\mathbf{b}_3$. They have Burgers vectors, ⅙, ⅙, and ⅙, respectively. By arranging the combination of these Shockley partial dislocations, ITB can be represented as different dislocation structures [59]. Molecular dynamics simulations and elastic analysis according to dislocation theory suggested a minimum energy interface that contains a repeatable sequence $\mathbf{b}_2$:$\mathbf{b}_1$:$\mathbf{b}_3$ on every {111} plane. The created ITB with such dislocations is consistent with the HRTEM observation [59]. In the absence of external stress, the compact ITB can spontaneously dissociate into two boundaries that are bonded with the 9R phase because of the reduction of dislocation core energy, i.e., one set of partials glide away from the initial compact ITB [62].

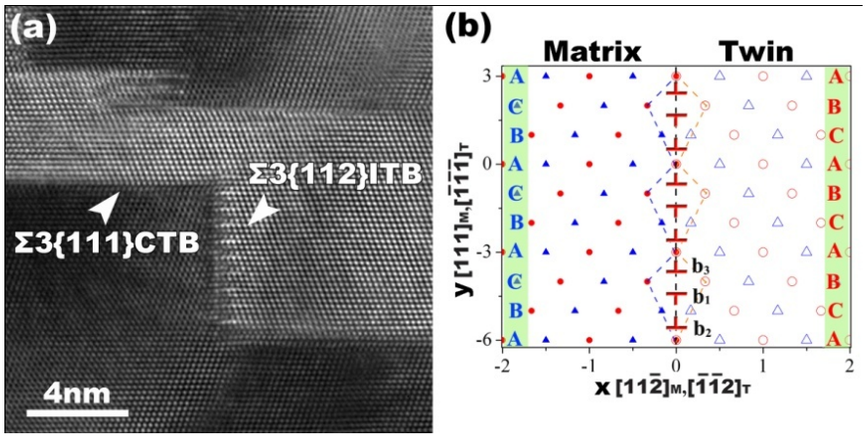

Figure 1. (a) HRTEM image showing atomic structures of both Σ3 {111} CTB and Σ3 {112} ITB. (b) A schematic illustration depicting the dislocation structure of Σ3 {112} ITB.

2.2. Migration of Σ3 {112} ITBs

By applying an in situ straining technique in a TEM, Σ3 {112} ITB migrates, corresponding to detwinning [60, 63]. Figure 2a shows the setup of a typical in situ nanoindentation experiment, where a nanotwinned Cu film is in contact with the W tip at the onset of an indentation test [60]. Three snapshots of the cross-sectional TEM (XTEM) micrographs, before indentation, at 33 seconds and at 55 seconds, show the migration of the two ITBs. The HRTEM micrograph in Figure 2e shows the migration unit, which is a 3-layer step and consistent with the unit of Σ3 {112} ITB.

The observed migration of Σ3 {112} ITBs thus can be explained from dislocation structure of the ITB. Atomistic simulations and topological model revealed that Σ3 {112} ITBs can be represented with a repeatable sequence $\mathbf{b}_2$:$\mathbf{b}_1$:$\mathbf{b}_3$ on every {111} plane that has net zero Burgers

vector [60, 63]. The attractive force between $\mathbf{b}_2$ and $\mathbf{b}_3$ groups them together to form paired partials. The partial dislocation $\mathbf{b}_1$ is easier to migrate than the paired partials because it experiences small Peierls barrier force [60, 63]. Under applied shear stress, the emitted partial dislocation $\mathbf{b}_1$ and the paired partials are subjected to the same magnitude but opposite-signed gliding force. Due to the high friction force on the paired partials, the dislocation $\mathbf{b}_1$ moves, meanwhile the interaction force drops. However, a load drop occurs around these dislocations due to the plastic strain associated with the motion of the dislocation $\mathbf{b}_1$, arresting the motion of the dislocation $\mathbf{b}_1$. The increasing stacking fault associated with the motion of dislocation $\mathbf{b}_1$ will pull the paired dislocations toward $\mathbf{b}_1$ until they again reach an equilibrium state.

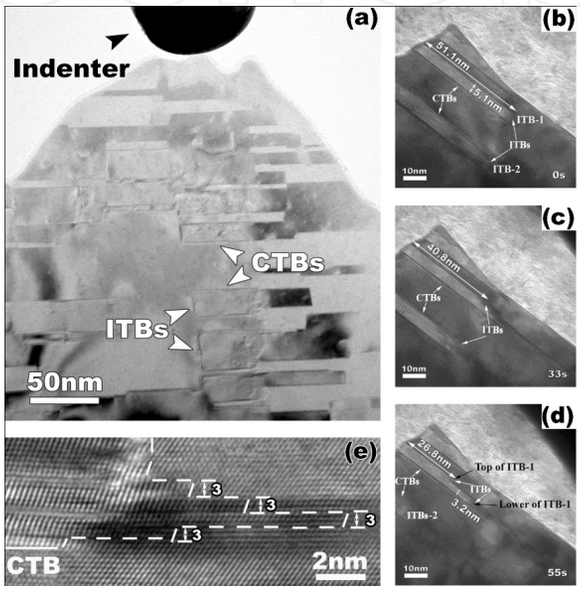

Figure 2. TEM images showing the migration of ITB in Cu. (a) Indentation tests, (b)-(d) three HRTEM images showing the position of Σ3 {112} ITB, and (e) the migration of Σ3 {112} ITB is accomplished via collective motion of three {111} atomic layers.

2.3. Dislocation-Σ3 {112} ITBs interactions

Figure 3 exhibits the dislocation-Σ3 {112} ITBs interaction and its influence on the migration of ITBs [61, 63]. In Figure 3a, we characterized an extended dislocation in the twin domain. After the dislocation entered into the ITB-1, we observed an emitted dislocation from the ITB-1 in the adjacent matrix (Figure 3b). Figure 3c shows the final structure of the ITB-1. Both its upper and lower sections have propagated towards the right, whereas the section that has a residual dislocation, $\mathbf{b}_r$, did not migrate. Using Burgers circuits we determine the Burgers vectors of incoming and emitted dislocations, respectively, while their line senses point into the paper. Figure 3d illustrates the dislocation-ITB interaction process. The incoming dislocation $\mathbf{b}_{in}$ glides on $\mathbf{B}_T\mathbf{A}_T\mathbf{C}_T$ (where T represents twin) and the Burgers vector could be either $\mathbf{B}_T\mathbf{A}_T$ or $\mathbf{B}_T\mathbf{C}_T$, since the screw component is invisible in the TEM image viewed along $\mathbf{A}_T\mathbf{C}_T$. The emitted dislocation $\mathbf{b}_{out}$ glides on ACD plane and with the Burgers vector **AD** or **CD**. Assuming the incoming dislocation has Burgers vector $\mathbf{B}_T\mathbf{A}_T$, the emitted dislocation should have Burgers vector **AD** or **CD**, minimizing the magnitude of the residual dislocation at the

http://dx.doi.org/10.5772/60880

ITB. The residual dislocation has the Burgers vector $\mathbf{b}_r = \mathbf{b}_{in} - \mathbf{b}_{out} = \mathbf{B}_T\mathbf{A}_T - \mathbf{AD} = \mathbf{AB} - \mathbf{AD} = \mathbf{DB}$, which can be seen as $\mathbf{D\delta} + \mathbf{\delta B}$. As a result, the residual Frank dislocation is sessile and cannot glide on any {111} planes in either twin or matrix. Therefore, the migration of the ITB has been restrained.

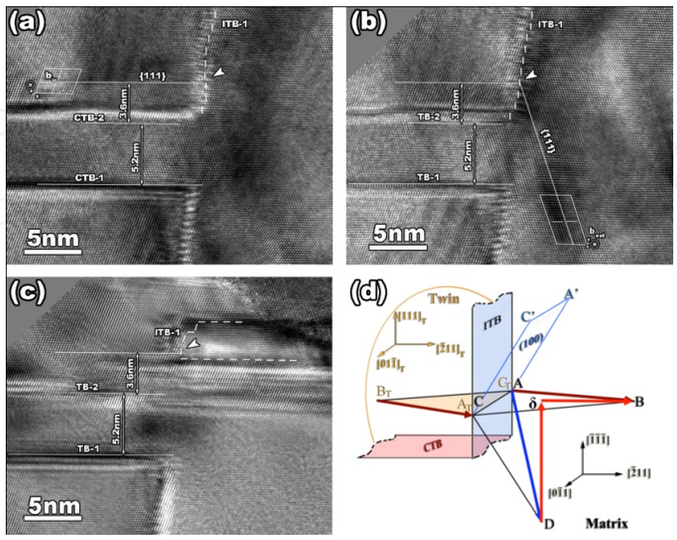

Figure 3. HRTEM images: (a) an extended dislocation in the twin domain and (b) an emitted dislocation in he matrix. The interaction position is indicated by the white arrow marks. $\mathbf{b}_{in}$, $\mathbf{b}_{out}$, and $\mathbf{b}_r$ are the incoming dislocation, the emitted dislocations, and the residual dislocation at ITB. (c) HRTEM image of the final stage of ITB-1 migration. The entire ITB has migrated except for the point at which slip transmission was observed. (d) Slip systems involved in slip transmission for a dislocation across ITBs.

2.4. Dislocation multiplication at coherent twin boundaries

Besides the well-known role of CTBs as barriers to block the movement of dislocations, in situ TEM experiments reveal a novel possibility that CTBs also facilitate the multiplication of Shockley partial dislocation [63, 64]. Figure 4 presents HRTEM snapshots of the interaction of a glide dislocation with a CTB, taken during dynamical loading. Figure 4a shows a HRTEM image—taken at 175.5s after the onset of the indentation experiment. Three dislocations close to the CTB are labeled as #1, #2, and #3. The stepped boundary suggests the formation of Shockley partial dislocations due to the interaction of glide dislocations with the CTB.

Corresponding to the configuration of the stepped coherent twin boundary, we labeled four segments as CTB-1, CTB-2, CTB-3, and CTB-4. During the observation period in the indentation experiment, we noticed that dislocations #1 and #2 and the segment CTB-1 did not move. For simplicity, CTB-1 is labeled as "0", corresponding to the reference position of the twin plane (Figure 4 a'). Under applied stress, we observed that the lattice dislocation #3 glides towards CTB-2, as identified in Figure 4 c. There is one extra {111} plane corresponding to the edge component of the dislocation normal to the CTB plane. During in situ TEM indentation test, the dislocation #3, a mixed 60° dislocation, glides towards the CTB. After 1 second, dislocation #3 entered the CTB-2. We observed one partial dislocation that is emitted into the adjacent matrix, and a sessile disconnection on the CTB (Figure 4b). Consequentially, we relabeled the CTB-2 with two segments separated by a sessile disconnection, the new segment is labeled as

CTB-2′. The most intriguing observation is that the CTB-2′ moves upward by three atomic planes (from -1 to +2), which implies that three Shockley partial dislocations nucleate and glide on the twin plane. Accompanying the migration of the CTB-2′, the CTB-3 also migrates upwards by five atomic planes (from -3 to +2), which is a result of the glide of the three newly nucleated Shockley partial dislocations. Figure 4d is one IFFT HRTEM snapshot, clearly showing a sharp step with the height of three {111} interplanar distances.

Corresponding to the change in the steps along the CTB, there are three possible mechanisms: (1) multiple transmission events of mixed dislocations, with each transmission producing one Shockley partial dislocation [65]; (2) nucleation of Shockley partial dislocations at the intersection of the CTB with the Σ3 {112} incoherent twin boundary (ITB) that runs almost vertically to the left of the HRTEM image in Figure 4a [60]; (3) multiple Shockley partial dislocations are generated due to the reaction of one lattice dislocation with the CTB. The first two mechanisms seem unlikely. First, TDs generated by multiple transmissions are unlikely to group together to form a sharp step due to their mutual repulsion [66, 67]. Secondly, if Shockley partial dislocations glide away from an adjoining ITB into the CTB, CTB-1 and CTB-2 would be displaced up or down by the same amount, more importantly, changing the positions of the dislocation #1 and #2 relative to the CTB-1.

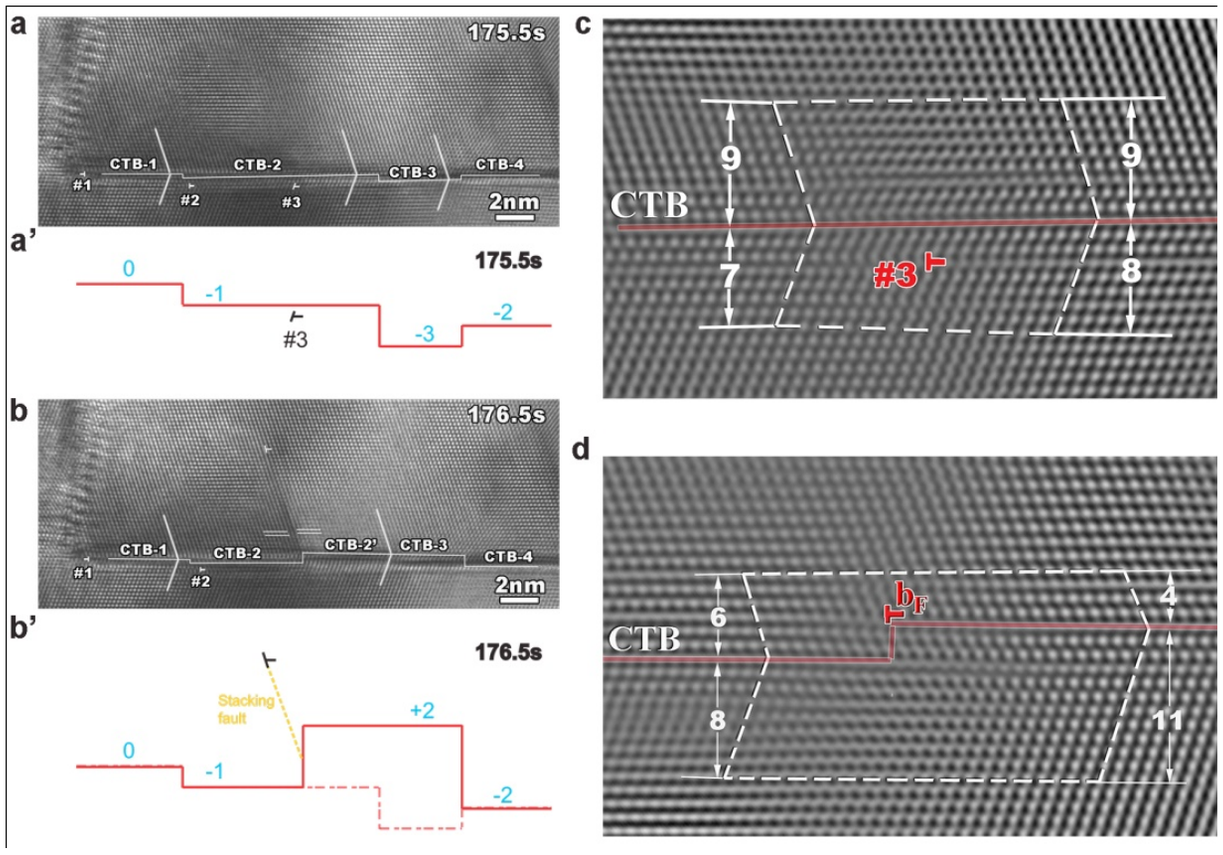

Figure 4. HRTEM images showing dislocation multiplication at a CTB. (a, a′) and (b, b′) illustrate the steps on the CTB before and after the dislocation-boundary reaction. Dislocation #1 and #2 did not move. The lattice dislocation #3 glides towards and enters CTB-2 after 1 second. (c) and (d) Magnified inverse fast Fourier transform (IFFT) HRTEM images showing dislocation #3 and a sharp step with the height of three {111} planes.

http://dx.doi.org/10.5772/60880

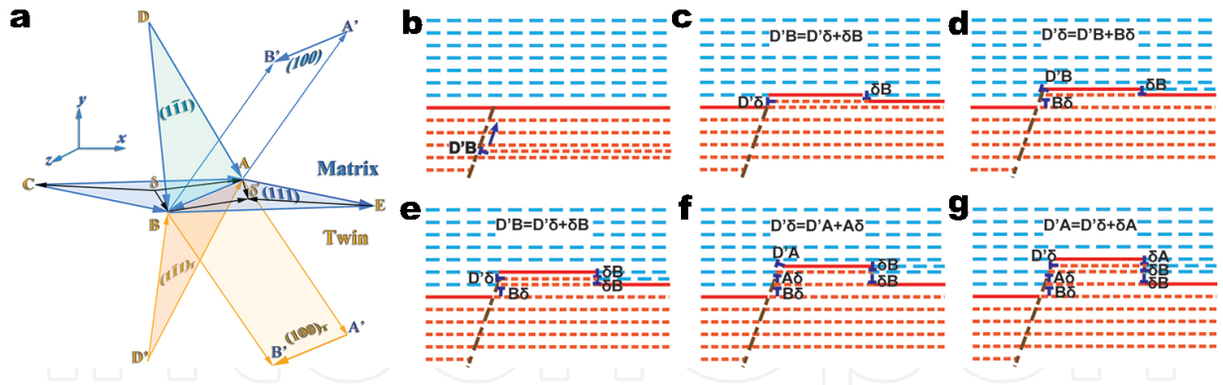

Figure 5. The orientation relation and several slip systems between twin and matrix. The CTB plane is defined as the (111) CBA plane with matrix above and twin below it. The *x*, *y*, and *z* directions are defined with respect to the matrix, along,, and, respectively. (b)-(g) Schematic illustration of the dislocation multiplication mechanism through the interaction of a mixed dislocation **D'B** with the twin boundary. A detailed description of the propagation process is given in the text.

The multiplication mechanism is schematically illustrated in Figure 5. The Thompson tetrahedron notation in Figure 5a shows the twin orientation relation and several slip systems that could be involved. The *x*, *y*, and *z* directions are defined with respect to the matrix, along,, and, respectively. Corresponding to the HRTEM image (Figure 4a), a full dislocation $\mathbf{b}_{in}$ with a ½<110> type Burgers vector (namely **D'B** in Figure 5a) on a {111} glide plane (namely in Figure 5a) glides towards the CTB (Figure 5b). Under compression due to the indentation, the suggested multiplication mechanism is presented as follows.

a. The lattice dislocation **D'B** glides towards the CTB (Figure 5b).

b. After the dislocation **D'B** encounters the CTB, it dissociates into a sessile Frank partial dislocation **D'δ** and a TD **δB**. The TD moves away from the intersection on the twin plane, resulting in the migration of the TB upwards by one atomic layer (Figure 5c). This initial dissociation had been confirmed in earlier MD simulations [34].

c. Once the partial **δB** moves away, the Frank partial **D'δ** could reassemble into a full dislocation accompanying the creation of a TD. This process is energetically un-favored. However, it could likely occur corresponding to plastic work and dislocation core reaction. Firstly, the dislocation core relaxes with a highly nonlinear energy change. The dissociation results new dislocations within a core dimension and the elastic energy is unchanged or slightly changed in the material. Secondly, the reassembly of a full dislocation from the Frank dislocation enables slip transmission, performing work. This reaction is very similar to that occurring at ratchet pole twinning generators and driven by the shear stress [68-71]. Correspondingly, the reaction is written as **D'δ = D'B + Bδ** or **D'δ = D'A+Aδ**. Once the dissociation is completed, the shear stress prevents the two partials **Bδ** and **δB** from annihilation, as shown in Figure 5 d.

d. The dislocation **D'B** then can experience a similar dissociation process as in (b) above. That is **D'B = D'δ + δB**. The shear stress causes the TD **δB** to move away, resulting in the migration of TB upward by one atomic layer (Figure 5e).

e. The residual dislocation **D'δ** can dissociate again as (c). However, with **Bδ** left by the 1st dissociation, the 2nd dissociation from **D'δ** to **D'A+Aδ** is favored energetically, as shown in Figure 5 f. The energy of the **Aδ/Bδ** pair, with a long-range energy equivalent to that of a single partial **δC** is much less than that of the pair 2**Bδ** that would result if the 2nd dissociation were D'δ to D'B+Bδ.

f. If the dislocation **D'A** dissociates into **D'δ** and **δA** again, and **δA** moves away under the shear stress, the twin boundary will migrate upward again by one atomic layer (Figure 5g). The left defect on the twin boundary is the sessile disconnection (**b** = **D'C**, h = height of three atomic layers), and **D'C** is the net of the three partials, **Bδ**, **Aδ**, and **D'δ**, respectively. The right defect on the twin boundary is the TD (**b** = **CB**, h = 3), and a net Burgers vector **CB** comprised of the partials δB, δB, and δA.

Accompanying with multiplication of Shockley partial dislocations at the CTB, the CTB will migrate upward and a stepped structure forms. The left comprises a step with an array of TDs in an alternating sequence **Bδ**: **Aδ**: **Bδ**: **Aδ**..., and one Frank partial **D'δ**. The right TD comprises a step with an array of TDs in a sequence of **δB**: **δB**: **δA**: **δB**: **δA**... on successive (111) planes. This mechanism provides a way to nucleate multiple TDs, causing the migration of CTBs. Of course, if the above operations are performed in the opposite sense, the twin boundary will migrate downward.

MD simulations were performed to further examine the multiplication mechanism proposed above. The simulation cell, shown in Figure 6a, contains about 24,000 Cu atoms with the coordinate systems of the x-axis along, the y-axis along, and the z-axis along. We initially disturb a group of atoms (10 atoms) with a displacement corresponding to half of a Shockley partial dislocation **δB** (Figure 6b). Figures 6c to 6e show several snapshots of nucleation and glide of two Shockley partial dislocations that form in accordance with the proposed mechanism. Accompanying the nucleation and glide of the dislocation **Bδ**, the Frank dislocation **D'δ** must locally shift upward as described previously, through a double-kink nucleation/core shuffle mechanism [65].

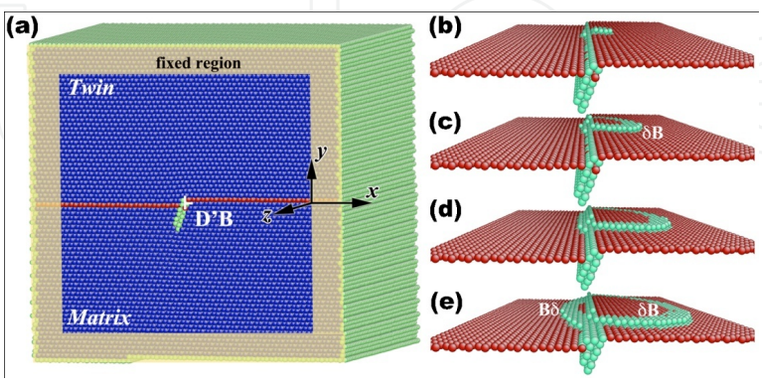

Figure 6. Molecular dynamics simulations: (a) Simulation cell, and four snapshots of the reaction mechanisms; (b) initial configuration (10 atoms are disturbed); (c) and (d) the nucleation and propagation of the TD δB; and (e) the glide of the other TD Bδ with the opposite sign in associated with the local climb of the dislocation D'B. Atoms are colored by common-neighbor-analysis. The red atoms represent stacking faults, relative to fcc.

http://dx.doi.org/10.5772/60880

3. Metallic interphase interfaces

Interfaces that act as sources, sinks, barriers, and storage sites for point and line defects strongly affect mechanical properties of materials [72-74]. Due to the controllability of dimensions and interface structures and properties, metallic multilayers that are synthesized using magnetic sputtering are good model systems to explore the effect of interfaces on the mechanical properties at different length scales ranging from nano- to micrometers [5, 10, 35, 75-89]. The strength of such metallic multilayers is significantly increased with decreasing layer thickness. Much of the mechanistic insights have been gained from computer simulations [13, 18, 90-93], but experimental measurements are limited to post mortem TEM of nano-indents, rolled, or fatigue samples [94-99]. Corresponding to the measured strength-layer thickness relation, the dominant deformation mechanisms in metallic multilayers have been postulated [5, 10] to vary with the layer thickness, from dislocation pile-up based Hall-Petch scaling law (layer thickness, $h \geq 50$ nm) to confined layer slip (CLS) (h around 5 ~ 50 nm), and ultimately to the interface resistance to single dislocation transmission ($h < 5$ nm). To elucidate the operation mechanisms of dislocations in multilayers at nanometer length scales, we performed in situ straining of Cu/Nb and Al/Nb multilayers in a TEM with the focus on interface structures, dislocation nucleation, dislocation climb, and interface shear resistance.

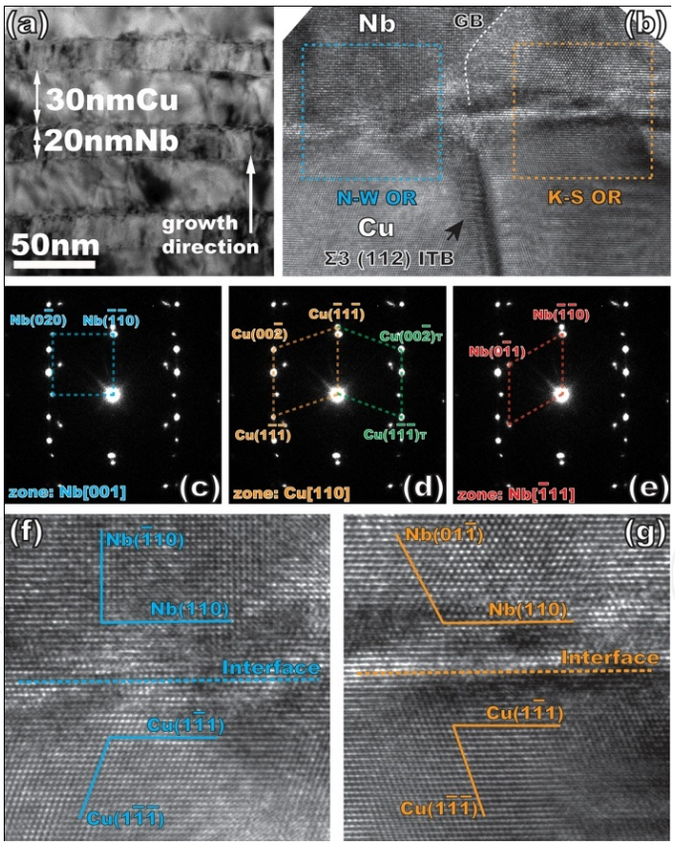

Figure 7. (a) Bright field TEM micrograph of Cu/Nb multilayer films with alternating layers of Cu (~30 nm) and Nb (~20 nm). (b) HRTEM image viewed from Cu [110], Nb [001] and Nb showing both K-S and N-W orientation relationships along Cu-Nb interface. (c)-(e) corresponding selected area diffraction pattern reveals Nb{110} || Cu{111} || Cu-Nb interface and twin orientation in Cu layer. (f) and (g) higher magnification images of N-W and K-S interface, respectively.

3.1. Interface structure

Bright field TEM micrograph of the cross-sectional view of the 20 nm Cu/Nb multilayers is shown in Figure 7 a. The interface is chemically sharp with no sign of intermixing. The dark shadow around interfaces is the strain contrast due to defects during the growth. The selected area diffraction patterns (SADP) shown in Figures 7 b-7dsuggest a quasi-single crystal film with a {110} Nb ||{111} Cu || interface plane. Diffraction pattern (DP) reveals that the Nb layers grow along <110> and the Cu layers grow along <111>. The DPs and the high-resolution TEM (HRTEM) images infer both Kurdjumov-Sacks (K-S, <001>Nb||<110>Cu) and Nishiyama-Wasserman (N-W, <111>Nb||<110>Cu) orientation relationships between Cu and Nb layers, as shown in Figures 7 f and 7g.

3.2. Dislocation nucleation

The in situ TEM has been performed at phase contrast imaging mode and explored the Shockley partial dislocations that nucleated at Cu/Nb interfaces. Figure 8a shows several stacking faults in Cu layers. With increasing strain, the stacking faults extend throughout the Cu layer as shown in Figures 8 b and 8c, and finally disappear, indicating that plastic deformation in Cu layers is carried over by full dislocations that nucleated from interfaces with the leading partial dislocation and trialing partial dislocation. Atomistic simulations have explored the nucleation mechanism of Shockley partial dislocations at interfaces, suggesting that the atomically flat KS interface can act as dislocation sources due to the presence of misfit dislocations [100]. In addition, during the indentation test, no deformation twins were observed even when the strain in some layers reaches ~50%, which is consistent with earlier post mortem TEM studies of rolled Cu-Nb multilayers [67, 101].

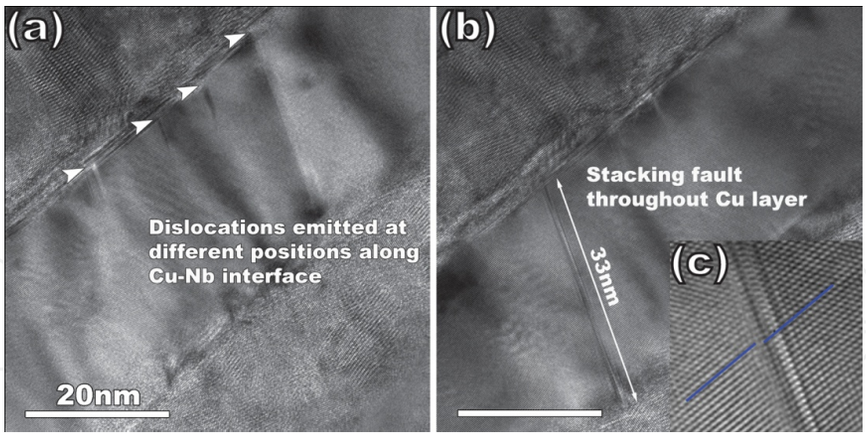

Figure 8. (a) HRTEM image shows several stacking faults generated in Cu, with the trailing partials trapped at Cu-Nb interface. (b) HRTEM image shows a stacking fault extending through the Cu layer. (c) Higher magnification image of the stacking fault in (b).

3.3. Confined layer slip

In situ nanoindentation is performed on the top surface of such multilayers under two-beam BF TEM mode, in which several threading dislocations with both ends pinned at the interfaces are seen as dark lines. However, images of loops gliding on the plane parallel to the electron

http://dx.doi.org/10.5772/60880

beam will not be visible. Figure 9 directly reveals the confined layer slip in both Cu and Nb layers. For simplicity, the discussion below is focused on observations made in the Cu layers. Two dislocations bow out under the applied stress as shown in Figure 9 a. With increasing stress, one new dislocation (marked as "III") nucleates and glides toward the same direction as the former two (Figure 9b) and two new dislocations (marked as "IV" and "V") nucleate and glide towards the opposite direction. With continuous compressive stress, the sixth dislocation (marked as "VI") nucleates. Four dislocations represented as blue dashed lines glide collectively towards the left, and the other two dislocations represented as yellow dashed lines glide towards the right. Since the TEM foil is under compressive stress, dislocations gliding to opposite directions should have opposite-signed Burgers vectors to each other. It is probable that two groups of dislocations glide on two different types of glide planes. As illustrated in Figure 9c', four dislocations with Burgers vector of **DB** glide to the left on a set of plane ABD, and the other two with opposite-signed Burgers vector glide towards the right on a set of plane BCD. Due to the frame rate limit of in situ TEM, there is another possible scenario regarding dislocations III and IV that belong to one loop expanding and then the threading arms moving in opposite directions but on the same plane.

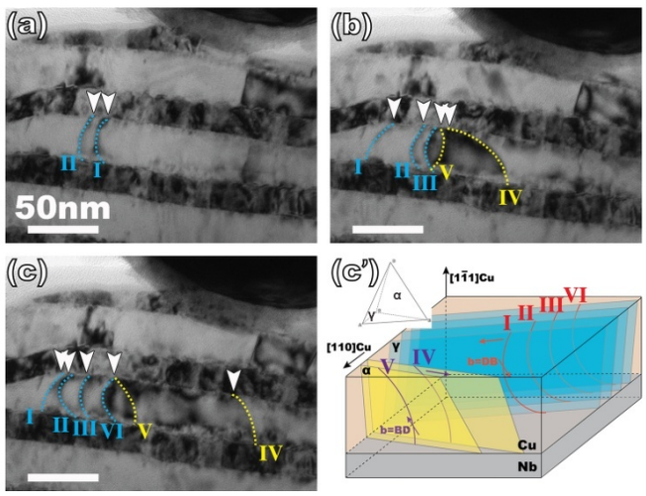

Figure 9. (a)-(c) A sequence of TEM movie images showing dislocation nucleation at Cu-Nb interfaces. Especially, two groups of dislocations glide in Cu layer towards opposite directions, which indicate they have opposite Burgers vector. (c') The corresponding schematic illustration shows the dislocations glide collectively on two sets of glide planes ABD and BCD.

3.4. Dislocations climb in interfaces

Figures 10a-d show a series of XTEM snapshots (processed by FFT) at different instants during a continuous loading process. Initially, two dislocations, labeled as $\mathbf{b}_1$ at the interface and $\mathbf{b}_2$ inside the Nb one atomic layer away from the interface, are separated by a distance, d_p, of 2.5 nm. d_p is measured along the direction parallel to the interface. After 2 seconds, d_p decreases to 1.7 nm as depicted in Figur 10b. The decrease in the separation distance via dislocation climb occurs at an average velocity of 0.4 nm/sec, two orders of magnitude larger than the climb velocity of dislocations in bulk Al lattice, ~0.001 nm/sec [102]. At 2.5 seconds, the two dislocations annihilate at the interface as shown in Fig. 10 c. The climb velocity is estimated to be 3.4 nm/sec, which is a lower bound estimation due to the big time step between frames. Finally, Figure 10d shows the annihilation of dislocations in the interface.

Dislocation climb involves mass transport via the absorption or emission of vacancies and/or interstitials [18, 103]. The climb rate depends on the concentration and diffusivity of point defects in the interface, in turn, depending on the formation energy of point defects [18, 90]. Figure 10e shows the mechanical work associated with the dislocation climb through the emission of one single vacancy as a function of the separation spacing *d*. When the vacancy formation energy is larger than the mechanical work (as discussed in Chapter 16 of *Theory of Dislocations*) [65], the dislocation climb is a thermal activated process [65]. Once the mechanical work is lower than the formation energy of vacancy, the climb becomes an athermal process with a sufficiently high rate. Corresponding to the formation energy of vacancy in bulk Al, 0.74 eV, we estimated the critical distance around 0.4 nm from the curve in Figure 10 e. However, the change of the climb velocity occurs at the distance of 1.7 nm (Figure 10b), suggesting that the athermal process begins below this critical distance. Correspondingly, we estimated the formation energy of vacancy from the curve (Figure 10e), 0.12 eV (a lower bound estimate). This energy is well in agreement with atomistic simulations [90].

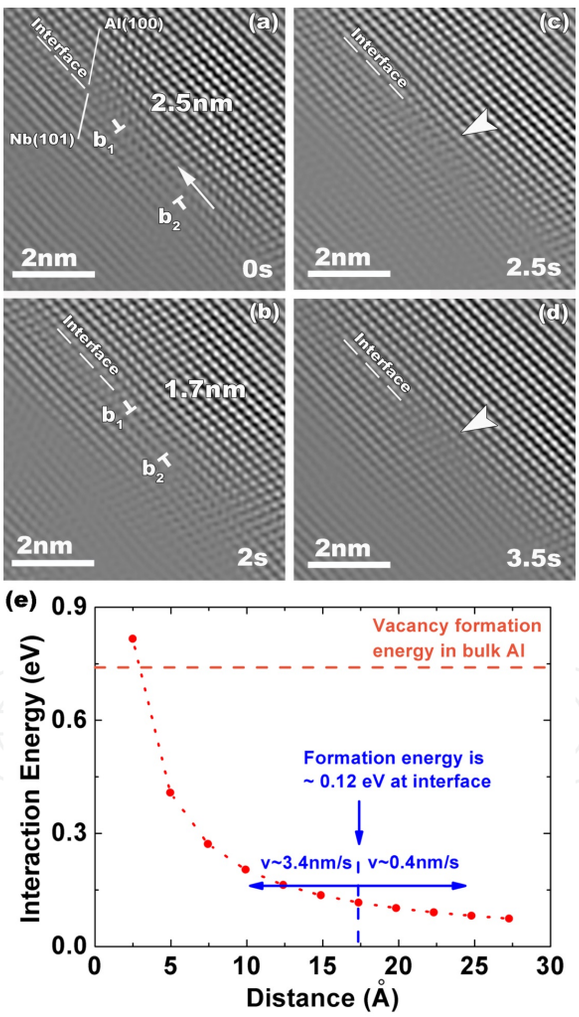

Figure 10. Dislocation annihilation process at Al/Nb interface. Two dislocations (a) with a separation of 2.4 nm at 0 second, (b) with a separation of 1.7 nm at 2 seconds, (c) annihilate each other at 2.5 seconds. (d) The interface becomes nearly perfect after dislocations annihilation At 3.5 seconds. (e) Mechanical work associated with the dislocation climb through the emission of one single vacancy from the dislocation as a function of the separation spacing *d*.

http://dx.doi.org/10.5772/60880

3.5. Interface shear strength

Using atomistic simulations, the critical stress corresponding to interfacial sliding is defined to be the interface shear strength [11, 104-107]. Molecular dynamics simulations have explored that Cu-Nb interface has a very low shear strength, significantly lower than the theoretical shear strengths of glide planes in perfect crystals of Cu and Nb [13, 108]. Using the push-out, full fragmentation and indentation tests in a SEM and TEM, people have measured interface strength (shearing and de-bonding) in experiments [5, 109-111]. However, the stress situation is rather complicated and thus many assumptions have to be made in interpreting experimental data.

Figure 11a shows the force versus displacement curve of an in situ compression test in TEM with compression axis at 25° off the pillar axis, while Figure 11b displays the starting microstructure. The sharp increase in load starting at the displacement of ~35 nm (Figure 11b) coincided with predominantly elastic behavior. At displacement of ~85 nm, load fluctuation was observed, indicative of the onset of dislocation activity. At this stage, the pre-existing dislocations might progressively glide out of the pillar and/or new dislocations might nucleate and glide from the interface and surfaces. At displacement of ~125 nm, the load steadily decreases. Comparing with the recorded video, we found that the steady decrease in force corresponds to the shearing of the pillar along the Cu-Nb interface. The microstructures immediately before and after failure are shown in Figure 11c and 11d.

We calculated the instantaneous shear stress at which the pillar failed, as shown in Fig. 11c'. The force is 63 uN and the Cu-Nb interface is 10° tilted away from the stage axis. The sheared Cu-Nb plane is approximately 224 nm in diameter. The critical shear strength of Cu-Nb interface is calculated to be 0.3 GPa. To ensure repeatability, several ex situ and in situ compression tests were performed, and the average shear strength of Cu-Nb interface is ~0.4 GPa among six tests, which is in good agreement with atomistic simulation [112] and evidences the concept of the easy nucleation and propagation of interfacial dislocations in a weak-shear interface [13, 113, 114].

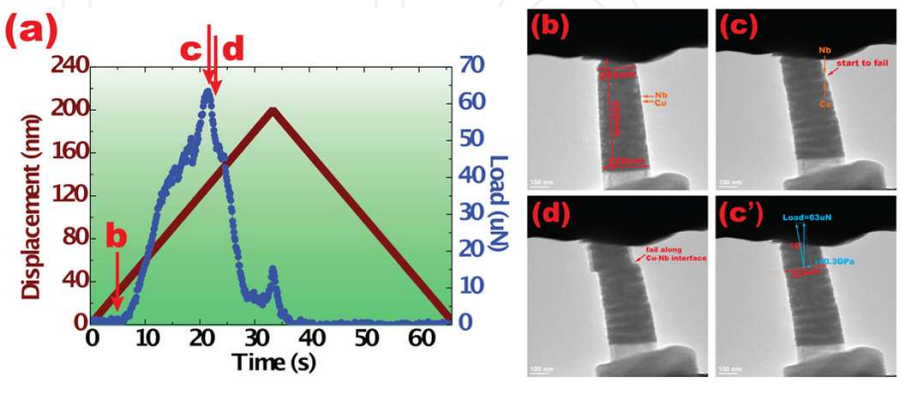

Figure 11. a) Force versus displacement curve of one typical pillar compression test. (b)-(d) Frames extracted from the video that correspond to the configuration of the pillar at the instances marked as b-d in (a), respectively. (c') displays the geometry relationship of compressed pillar with the indenter right before failure.

4. Metal/ceramic interfaces

Metal/ceramic multilayers with promising mechanical, physical, and chemical properties have been practically used in a wide range of temperatures, mechanical loadings, and environmental conditions [115-117]. One primary scientific interest stems partly from the large difference in strength and ductility between their constituent phases. By combining the two constitutes into a composite, the stronger constitute strengthens the composites while the ductile constitute make the composites ductile. In general, the mechanical properties of such composites have a low strength than the stronger constitute and a low ductility than the ductile constitute [118-132]. Ceramics are lacking in room temperature plasticity and fracture toughness [118, 119], although localized dislocation activity in ceramics at room temperature has been observed underneath the indenter [120-122]. However, for layered composites particularly with the individual layer thickness less than a few nanometers, both strength and ductility could be improved. Recent micro-pillar tests revealed plastic co-deformability in Al-TiN multilayers as the layer thickness less than 5 nm [133, 134]. In this section, we present our recent in situ TEM work on Al-TiN multilayers with various layer thicknesses, 50 nm, 5 nm and 2.7 nm, exploring the effect of reduced layer thickness on metal-ceramic plastic co-deformability [135].

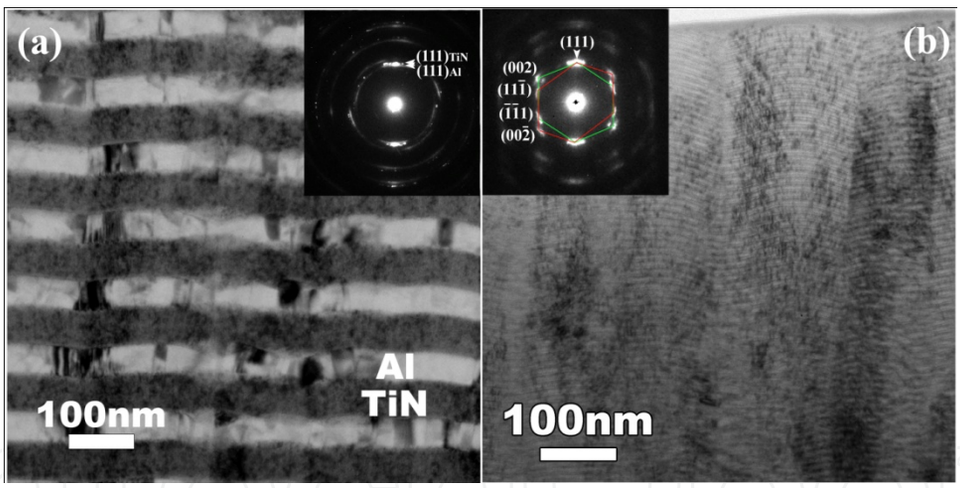

Figure 12. TEM images of the as-deposited films with the individual layer thickness (a) 50 nm and (b) 5 nm.

4.1. Interface structures

TEM images of the as-deposited films with the individual layer thickness 50 nm and 5 nm are shown in Figure 12. We characterized the orientation relation between the Al and TiN layers according to the diffraction patterns (DPs): (111)Al||(111)TiN||interface and <110>Al||<110>TiN. The DPs indicate the epitaxial growth of Al and TiN within a column and the growth direction along <111>. The DP in Figure 2b also suggests that grains in a column may be misoriented with respect to each other by 60°, resulting in the formation of Σ3{112} incoherent twin boundaries (ITBs), as shown in Figure 13.

http://dx.doi.org/10.5772/60880

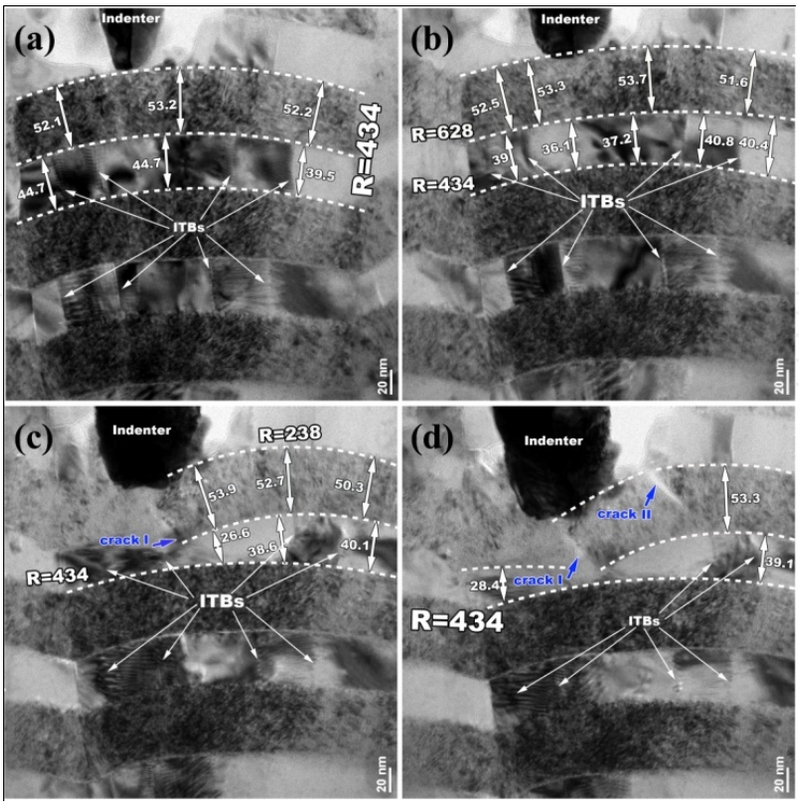

Figure 13. TEM images of the 50 nm Al-50 nm TiN multilayer during in situ indentation, showing the thickness reduction in the Al layers and cracks in the first TiN layer. Σ3{112} ITBs are present in the Al layers and migrate during indentation.

4.2. Deformation mechanism at large individual layer thickness (≥ 50 nm)

Four TEM images of the 50 nm Al-50 nm TiN multilayer during in situ indentation in Figure 13 show the thickness reduction in the Al layers and cracks in the first TiN layer and cracks in the first TiN layer. Being consistent with the DP in figure 12b, Σ3 {112} ITBs were identified in Al layers in one column (Figure 13a). During indentation testing, we observed that the thickness of the first Al layer beneath the indenter reduces from 45 nm to 37 nm to 27 nm (Figures 13a-c). Figures 14a and 14b show high-resolution TEM (HRTEM) images of Al-TiN interfaces before and after indentation. A low angle tilt boundary with the tilt angle of 9.4º was observed in the deformed Al-TiN interface, which is ascribed to the pileup of dislocations in the Al layer along the interface. However, the TiN layers are mainly subjected to elastic deformation and no detectable thickness reduction is measured in Figure 13. Consequently, we observed the first crack that is initiated in the TiN layer from the Al-TiN interface (Figures 13c and 14b) and the second crack that is initiated in the TiN layer from the top surface (Figures 13d and.14c). According to the crystallography of the TiN layer, the second crack surface is close to a {111} plane (Figure 14c). It is worthy of mentioning that the Al layer does not fracture associated with the opening of the crack (Figure 14d). Using finite element method we further studied the stress state associated with the crack initiation and found that both the cracks are initiated by the tensile stress (Figure 15).

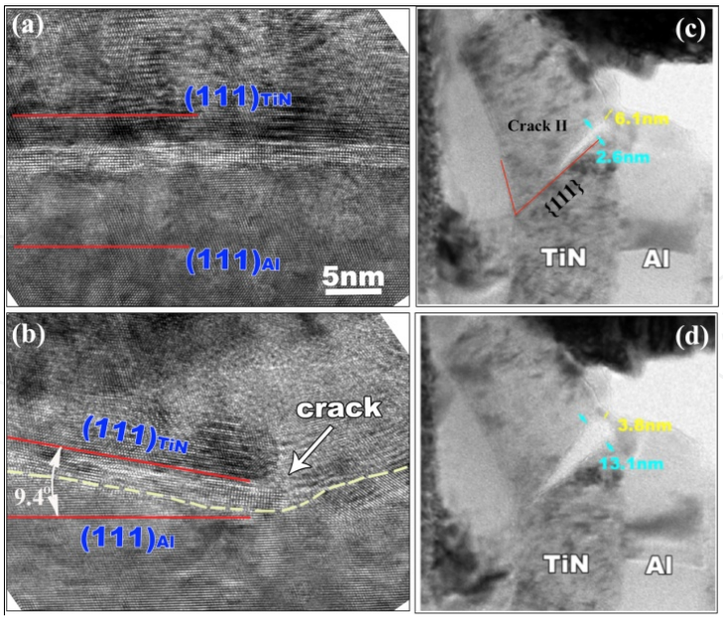

Figure 14. (a) and (b) HRTEM images of the Al-TiN interface before and after indentation. The red lines indicate the (111) plane. (c) and (d) Initiation and propagation of the crack II. The Al layer near the crack II does not fracture and the layer thickness reduces from 6.1 nm to 3.8 nm.

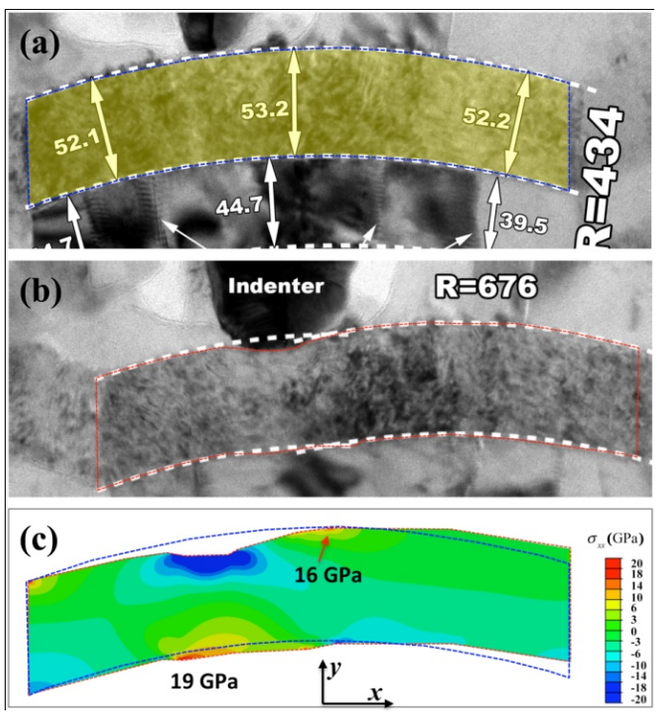

Figure 15. The change in the morphology of the first TiN layer during indentation, (a) the initial shape of the TiN layer before indentation and (b) the deformed TiN layer before cracking. The stress field was solved in the TiN layer with the displacement boundary condition, which is determined according to the morphology change from (a) to (b). The Young's modulus is 260 GPa and the Poisson's ratio is 0.30. Two high tensile stress regions are corresponding to the crack initiation.

http://dx.doi.org/10.5772/60880

4.3. Deformation mechanism when layer thickness is small (≤ 5 nm)

Plastic co-deformation was observed in the 5 nm Al-5 nm TiN multilayers and the 2.7 nm Al-2.7 nm TiN multilayer during in situ indentation. For the 5 nm Al-5 nm TiN multilayer, a significant plastic deformation beneath the indenter was measured in the first and second Al layers according to the change in layer thickness. Associated with the bending of the first TiN layer, the second Al layer reduces layer thickness from ~5.5 nm to ~1.9 (Figures 16a and 16b). The local radius of the first TiN layer beneath the indenter decreases from the initial infinity to the range of 102 ~ 156 nm (Figure 16b) and a slight reduction of the first TiN layer thickness is evidenced in the HRTEM images (Figures 16d and 16e) from 5.87 nm to 5.02 nm. Figure 16c shows the HRTEM image of a tilt boundary that is associated with the high density of dislocations in the Al layer and dislocation pile-up along the Al-TiN interface. Plastic deformation in TiN layers is achieved with the dislocations motion that is characterized in the TiN layer by the Burgers circuit (Figure 16f).

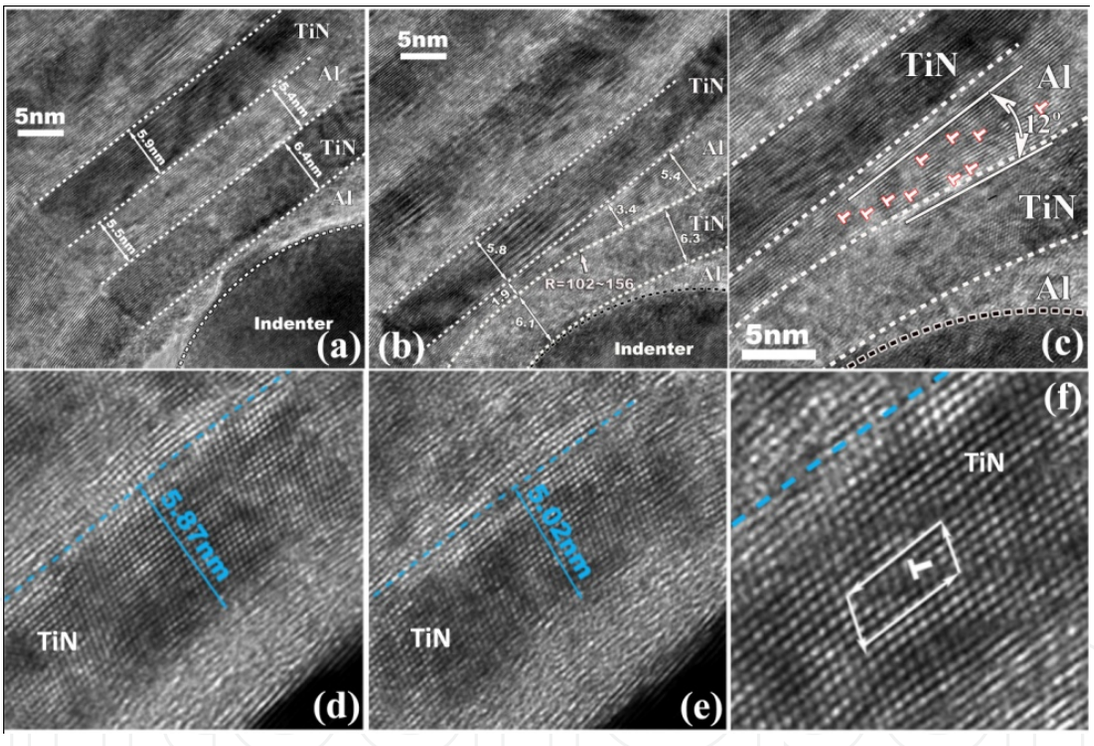

Figure 16. Plastic co-deformation in the 5 nm Al-5 nm TiN multilayers. (a) and (b) TEM images showing the reduction of thickness in the second Al layer. (c) A tilt boundary between the first TiN layer and the second Al layer, which is associated with the accumulation of dislocations in the Al layer and at the interface. Plastic deformation in the first TiN layer, (d) and (e) show the thickness reduction from 5.87 nm to 5.02 nm, and (f) a lattice dislocation identified by the Burgers circuit.

For the 2.7 nm Al-2.7 nm TiN multilayer, Figure 17c shows a highly coherent interface structure between the Al and TiN layers, this is due to the small lattice difference between Al and TiN and the fine layer thickness. During the film growth, Al atoms have a high diffusivity on Al (111) surface, facilitating the epitaxial growth of a flat Al layer. Consequently, the TiN layer will grow on a flat Al surface (111) and a sharp and flat Al-TiN interface forms. However, the

low diffusivity in the TiN layer may result in a relatively rough TiN (111) surface. The newly formed TiN-Al interface is relatively rough, reducing the contrast in terms of the coherent strain. Thus, the sharp Al-TiN interface benefits us to distinguish a bi-layer thickness (Figure 17c). A huge plastic deformation was measured according to the change in the first five bi-layers beneath the indenter, the thickness reduction in the first three bi-layers from 17.5 nm to 6.3 nm, corresponding to a strain of -64% (Figure 17d and 17e).

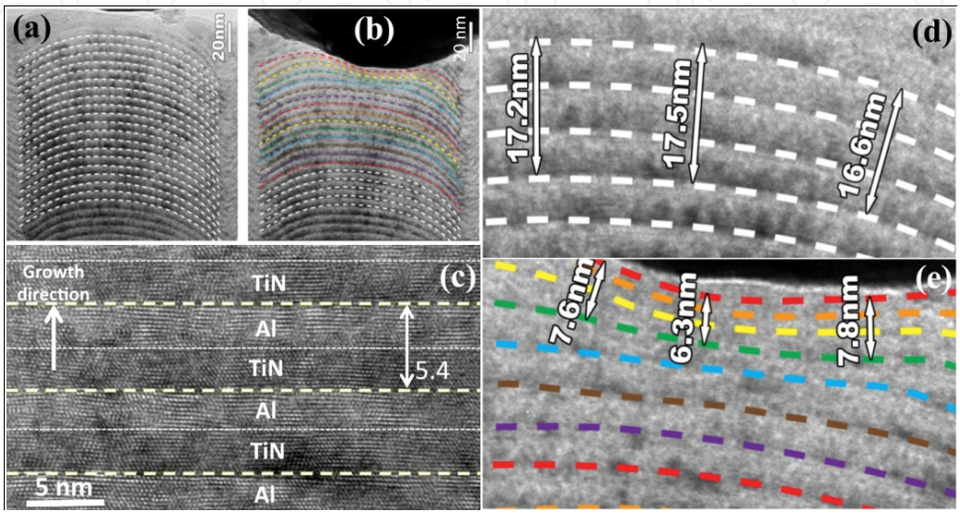

Figure 17. The 2.7 nm Al-2.7 nm TiN multilayer before (a) and during indentation (b). The bold dashed lines indicate the Al-TiN interfaces and the thin dashed indicate the TiN-Al interfaces. (d) and (e) Plastic deformation in first three bilayers corresponds to the thickness reduction from 17.5 nm to 6.3 nm.

5. Summary

Using in situ TEM, we studied the interactions of dislocations with three types of interfaces: (i) twin boundaries in Cu; (ii) metallic interphase boundaries; and (iii) metal/ceramic interfaces. For twin boundaries in face centered cubic structure, we characterized Σ3 {112} ITB with repeatable units of three Shockley partial dislocations. Such dislocation structure thus corresponds to detwinning of nanotwins, which is accomplished via stress-induced collective migration of Σ3 {112} ITB. When lattice gliding dislocations transmit across a Σ3 {112} ITB, we found that such transmission locally changes the dislocation structure of ITBs thereby pinning it against migration to higher levels of stress. More importantly, when a glide dislocation enters a Σ3 {111} CTB, Shockley partial dislocations can be multiplied via the dissociation of lattice dislocation. The fundamental understanding of the deformation behavior of metallic layered nanocomposites has been explored through in situ TEM observation: (1) the Cu-Nb interface acts as the preferred nucleation sites for glide dislocations and both Cu and Nb layers co-deform to large plastic strains without cracking via confined layer slip; (2) the Al/Nb interfaces can facilitate dislocation climb through vacancy diffusion, which result in the recovery of dislocation contents within interfaces, in agreement with the experimental observation in the

rolling of Cu/Nb multilayers; and (3) the Cu/Nb interface exhibits the low shear strength in the range of 0.3 to 0.55 GPa, and correspondingly, the plastic deformation may be localized along the interfaces when the shear stress on interface plane corresponding to any loading conditions reaches the interface shear strength. For metal-ceramics interface, a significant plastic co-deformation is only observed for the layer thickness in a few nanometers. For the layer thickness 5 nm and 2.7 nm, plastic deformation in TiN layer was measured according to the layer thickness reduction and plastic deformation mechanism was characterized with glide dislocations that have been identified in HRTEM images. For example in the 2.7 nm Al-2.7 nm TiN multilayer, the first five Al-TiN bi-layers beneath the indenter tip experience a significant elastic-plastic deformation of ~60% without detectable cracks, while retaining the interface plane orientation (111)Al||(111)TiN consistent with compatible plasticity between the Al and TiN layers.

Author details

Nan Li[1] and Jian Wang[1,2*]

*Address all correspondence to: wangj6@lanl.gov

1 Los Alamos National Laboratory, Los Alamos, NM, USA

2 Mechanical and Materials Engineering, University of Nebraska-Lincoln, Lincoln, NE, USA

References

[1] A. Misra, A. Gibala. Metall. Mater. Trans. A 30A, 991 (1999).

[2] R.G. Hoagland, T.E. Mitchell, J.P. Hirth, H. Kung. Philos. Mag. 82, 643 (2002).

[3] S.J. Zheng, I.J. Beyerlein, J.S. Carpenter, K. Kang, J. Wang, W.Z. Han, N.A. Mara. Nat. Commun. 4, 1696 (2013).

[4] I.J. Beyerlein, N.A. Mara, J.S. Carpenter, T. Nizolek, W.M. Mook, T.A. Wynn, R.J. McCabe, J.R. Mayeur, K. Kang, S.J. Zheng, J. Wang, M.P. Tresa. J. Mater. Res. 28, 1799 (2013).

[5] J. Wang, A. Misra. Curr. Opin. Solid State Mater. Sci. 15, 20 (2011).

[6] W.D. Sproul. Science 273, 889 (1996).

[7] B.M. Clemens, H. Kung, S.A. Barnett. MRS Bull. 24, 20 (1999).

[8] A. Misra, H. Kung. Adv. Eng. Mater. 3, 217 (2001).

[9] M.A. Phillips, B.M. Clemens, W.D. Nix. Acta Mater. 51, 3171 (2003).

[10] A. Misra, J.P. Hirth, R.G. Hoagland. Acta Mater. 53, 4817 (2005).

[11] J. Wang, R.G. Hoagland, J.P. Hirth, A. Misra. Acta Mater. 56, 5685 (2008).

[12] R.G. Hoagland, R.J. Kurtz, C.H. Jr Henager. Scr. Mater. 50, 775 (2004).

[13] J. Wang, R.G. Hoagland, A. Misra. Scr. Mater. 60, 1067 (2009).

[14] J. Wang, R.G. Hoagland, J.P. Hirth, A. Misra. Acta Mater. 56, 3109 (2008).

[15] M.J. Demkowicz, J. Wang, R.G. Hoagland, Dislocations in Solids, vol. 14, pp. 141-207 (chap.83). Editor: Hirth, J.P. Amsterdam: Elsevier North-Holland (2008).

[16] P.M. Derlet, P. Gumbsch, R.G. Hoagland, J. Li, D.L. McDowel, H. Van Swygenhoven, J. Wang. MRS Bull. 34, 184 (2009).

[17] X.Y. Liu, R.G. Hoagland, J. Wang, T.C. Germann, A. Misra. Acta Mater. 58, 4549 (2010).

[18] J. Wang, R.G. Hoagland, A. Misra. Appl. Phys. Lett. 94, 131910 (2009).

[19] J. Wang, A. Misra, R.G. Hoagland, J.P. Hirth. Acta Mater. 60, 1503 (2012).

[20] S. Shao, J. Wang, A. Misra, R.G. Hoagland. Sci. Rep. 3, 2448 (2013).

[21] I.J. Beyerlein, J. Wang, K. Kang, S.J. Zheng, N.A. Mara. Mater. Res. Lett. 1, 89 (2013).

[22] C.A. Bronkhorst, S.R. Kalidindi, L. Anand. Philos. Trans. R. Soc. Lond. A 341, 443 (1992).

[23] H.M. Mourad, K. Garikipati. Comput. Methods Appl. Mech. Eng. 196, 595 (2006).

[24] M.R. Tonks, J.F. Bingert, C.A. Bronkhorst, E.N. Harstad, D.A. Tortorelli. J. Mech. Phys. Solids 57, 1230 (2009).

[25] H. Wang, P.D. Wu, C.N. Tome, J. Wang. Mater. Sci. Eng. A 555, 93 (2012).

[26] H. Wang, P.D. Wu, J. Wang, C.N. Tome. Int. J. Plast. 49, 36 (2013).

[27] H. Wang, P.D. Wu, J. Wang. Int. J. Plast. 47, 49 (2013).

[28] H. Wang, P.D. Wu, C.N. Tome, J. Wang. Int. J. Solids Struct. 49, 2155 (2012).

[29] J. Wang. JOM 63 (9), 57 (2011).

[30] J.W. Christian, S. Mahajan. Prog. Mater. Sci., 39, 1 (1995).

[31] L. Lu, X. Chen, X. Huang, K. Lu. Science 323, 607 (2009).

[32] L. Lu, Y. Shen, X. Chen, L. Qian, K. Lu, Science 304, 422 (2004).

[33] E. Ma, M. Wang, Q.H. Lu, M.L. Sui, L. Lu, K. Lu. Appl. Phys. Lett. 85, 4932 (2004).

[34] X.Y. Li, Y.J. Wei, L. Lu, Ke Lu, H. J. Gao. Nature 464, 877 (2010).

[35] T. Zhu, Ju Li. Prog. Mater. Sci. 55, 710 (2010).

[36] X. Zhang, H. Wang, X.H. Chen, L. Lu, K. Lu, R.G. Hoagland, A. Misra. Appl. Phys. Lett. 88, 173116 (2006).

[37] O. Anderoglu, A. Misra, H. Wang, X. Zhang. J. Appl. Phys. 103, 094322 (2008).

[38] X. Zhang, A. Misra, H. Wang, J.G. Swadener, A.L. Lima, M.F. Hundley, R.G. Hoagland. Appl. Phys. Lett. 87, 233116 (2005).

[39] M. Dao, L. Lu, Y.F. Shen, S. Suresh. Acta Mater. 54, 5421 (2006).

[40] O. Anderoglu, A. Misra, H. Wang, F. Ronning, M.F.Hundley, X. Zhang. Appl. Phys. Lett. 93, 083108 (2008).

[41] X. Zhang, O. Anderoglu, R.G.Hoagland, A. Misra. JOM 60 (9), 75 (2008).

[42] C.J. Shute, B.D. Myers, S. Xie, S.-Y. Li, T.W. Barbee, Jr., A.M. Hodge, J.R. Weertman. Acta Mater. 59, 4569 (2011).

[43] V. Yamakov, D. Wolf, S. R. Phillpot, A. K. Mukherjee, H. Gleiter, Nature Mater. 3, 43 (2004).

[44] V. Yamakov, D. Wolf, S.R. Phillpot, H. Gleiter. Acta Mater. 50, 5005 (2002).

[45] K.S. KumarH. Van Swygenhoven, S. Suresh. Acta Mater. 51, 5743 (2003).

[46] H. van Swygenhoven, P.M. Derlet, A.G. Frøseth. Nature Mater. 3, 399 (2004).

[47] O. Anderoglu, A. Misra, J. Wang, R.G. Hoagland, J.P. Hirth, X. Zhang. Int. J. Plast. 26, 875 (2010).

[48] J. Wang, H. Huang. Appl. Phys. Lett. 88, 203112 (2006).

[49] T. Zhu, J. Li, A. Samanta, H.G. Kim, S. Suresh. Proc. Natl. Acad. Sci. U.S.A. 104, 3031 (2007).

[50] K.A. Afanasyev, F. Sansoz. Nano Lett. 7, 2056 (2007).

[51] Z.H. Jin, P. Gumbsch, K. Albe, E. Ma, K. Lu, H. Gleiter, H. Hahn. Acta Mater., 56, 1126 (2008).

[52] T.C. Lee, I.M. Robertson, H.K. Birnbaum. Philos. Mag. A 62, 131 (1990).

[53] T.C. Lee, I.M. Robertson, H.K. Birnbaum. Metall. Trans. A 21A, 2437 (1990).

[54] Y.B. Wang, M.L. Sui. Appl. Phys. Lett. 94, 021909 (2009).

[55] J.K. Rittner, D.N. Seidman, K.L. Merkle. Phys. Rev. B 53, R4241 (1996).

[56] G. Lucadamo, D.L. Medlin. Science 300, 1272 (2003).

[57] D.L. Medlin, G.H. Campbell, C.B. Carter. Acta Mater. 46, 5135 (1998).

[58] J.A. Brown, N.M. Ghoniem. Acta Mater. 57, 4454 (2009).

[59] J. Wang, O. Anderoglu, J.P. Hirth, A. Misra, X. Zhang. Appl. Phys. Lett. 95, 021908 (2009).

[60] J. Wang, N. Li, O. Anderoglu, X. Zhang, A. Misra, J.Y. Huang, J.P. Hirth. Acta Mater. 58, 2262 (2010).

[61] N. Li, J. Wang, J.Y. Huang, A. Misra, X. Zhang. Scr. Mater. 64, 149 (2011).

[62] J. Wang, A. Misra, J.P. Hirth. Phys. Rev. B 83, 064106 (2011).

[63] N. Li, J. Wang, X. Zhang, A. Misra. JOM 63(9), 62 (2011).

[64] N. Li, J. Wang, A. Misra, J.Y. Huang, J.P. Hirth. Acta Mater. 59, 5989 (2011).

[65] J. P. Hirth, J. Lothe, Theory of dislocations. New York: Wiley; 1982.

[66] C.H. Jr Henager, R.J. Kurtz, R. G. Hoagland. Philos. Mag. 84, 2277 (2004).

[67] A. Misra, J. P. Hirth, R. G. Hoagland, J. D. Embury, H. Kung. Acta Mater. 52, 2387 (2004).

[68] R. Priestner, W. C. Leslie. Philos. Mag. 11, 895 (1965).

[69] Z. S. Basinski, M. S. Szczerba J. D. Embury. In: Yoo MH, Wuttig M, editors. Twinning in advanced materials. Warrendaale, PA: TMS 1994.

[70] K.P. D. Lagerlof, J. Castaing, P. Pirouz, A. H. Heuer. Philos. Mag. 82A, 2841 (2002).

[71] Y.T. Zhu, X.L. Wu, X.Z. Liao, J. Narayan, L.J. Kecskes, S.N. Mathaudhu. Acta Mater. 59, 812 (2011).

[72] A.P. Suutton, R.W. Balluffi. *Interfaces in crystalline materials*. Oxford: Oxford University Press (1995).

[73] J.P. Hirth. Metall Trans 3, 3047 (1972).

[74] N. Li, J. Wang, A. Misra, J.Y. Huang. Microscopy and Microanalysis 18, 1155 (2012).

[75] A. Misra, M. Verdier, Y. C. Lu, H. Kung, T. E. Mitchell, M. Nastasi. Scr. Mater. 39, 555 (1998).

[76] P.M. Anderson, C. Li. Nanostruct Mater. 5, 349 (1995).

[77] P.M. Anderson, T. Foecke, P. M. Hazzledine. MRS Bull 24, 27 (1999).

[78] P.M. Anderson, J. S. Carpenter. Scr. Mater. 62, 325 (2010).

[79] L.H. Friedman, D.C. Chrzan. Phys. Rev. Lett. 81, 2715 (1998).

[80] C.S. Pande, R. A. Masumura, R.W. Armstrong. Nanostruct Mater. 2, 323 (1993).

[81] I.J. Beyerlein, J. Wang, R. Zhang. Acta Mater. 61, 7488 (2013).

[82] S.I. Rao, P.M. Hazzledine. Philos. Mag. A 80, 2011 (2000).

[83] C. H. Jr Henager, R. J. Kurtz, R.G. Hoagland. Philos. Mag. 84, 2277 (2004).

[84] J.P. Hirth, R.C. Pond, R.G. Hoagland, X.Y. Liu, J. Wang. Prog. Mater. Sci. 58, 749 (2013).

[85] I.J. Beyerlein, J. Wang, K. Kang, S.J. Zheng, N.A. Mara. Mater. Res. Lett. 1, 89 (2013).

[86] W.D. Nix. Metall Trans A 20A, 2217 (1989).

[87] J. Wang, R.F. Zhang, C.Z. Zhou, I.J. Beyerlein, A. Misra. Int. J Plast. 53, 40 (2014).

[88] N. Abdolrahim, I.N. Mastorakos, H.M. Zbib. Phys. Rev. B 81, 054117 (2010).

[89] N.R. Overman, C.T. Overman, H.M. Zbib, D.F. Bahr. J. Eng. Mater. Technol. 131, 041203 (2009).

[90] M.J. Demkowicz, R.G. Hoagland, J.P. Hirth. Phys. Rev. Lett. 100, 136102 (2008).

[91] R.G. Hoagland, J.P. Hirth, A. Misra, Philos. Mag. 86, 3537 (2006).

[92] S.S. Quek, Y. Xiang, Y. W. Zhang, D. J. Srolovitz, C. Lu. Acta Mater. 54, 2371 (2006).

[93] S.S. Quek, Y. W. Zhang, Y. Xiang, D. J. Srolovitz. Acta Mater. 58, 226 (2010).

[94] N.A. Mara, D. Bhattacharyya, P. Dickerson, R. G. Hoagland, A. Misra. Appl. Phys. Lett. 92, 231901 (2008).

[95] N.A. Mara, D. Bhattacharyya, J. P. Hirth, P. Dickerson, A. Misra. Appl. Phys. Lett. 97, 021909 (2010).

[96] I.J. Beyerlein, N. A. Mara, D. Bhattacharyya, D. J. Alexander, C. T. Necker. Int. J. Plast. 27, 121 (2010).

[97] P.M. Anderson, J.F. Bingert, A. Misra, J.P. Hirth. Acta Mater. 51, 6059 (2003).

[98] X. F. Zhu, B. Zhang, J. Gao, G. P. Zhang. Scr. Mater. 60, 178 (2009).

[99] Y. P. Li, G. P. Zhang. Acta Mater. 58, 3877 (2010).

[100] R. F. Zhang, J. Wang, I. J. Beyerlein, T. C. Germann. Scr. Mater. 65, 1022 (2011).

[101] A. Misra, X. Zhang, D. Hammon, R. G. Hoagland. Acta Mater. 53, 221 (2005).

[102] N. Li, J. Wang, J.Y. Huang, A. Misra, X. Zhang. Scr. Mater. 63, 363 (2010).

[103] E.G. Fu, N. Li, A. Misra, R.G. Hoagland, H. Wang, X. Zhang. Mater. Sci. Eng. A 493, 283 (2008).

[104] J. Wang, C. Zhou, I. J. Beyerlein, S. Shao. JOM 66(1), 102 (2014).

[105] F. Sansoz, J.F. Molinari. Scr. Mater. 50, 1283 (2004).

[106] S. Ogata, J. Li, S. Yip. Science 298, 807 (2002).

[107] S. Ogata, N. Hirosaki, C. Kocer, Y. Shibutani. J. Mater. Res. 18, 1168 (2003).

[108] N.I. Medvedeva, Y.N. Gornostyrev, O.Y. Kontsevoi, A.J. Freeman. Acta Mater. 52, 675 (2004).

[109] P.J. Withers, J.A. Bennett, M. Kuroda. Acta Mater. 58, 6090 (2010).

[110] T.E. Matikas. Adv. Compos. Mater. 17, 75 (2008).

[111] N. Li, N.A. Mara, J. Wang, P. Dickerson, J.Y. Huang, A. Misra. Scr. Mater. 67, 479 (2012).

[112] Z. Shen, R.H. Wagoner, W.A.T. Clark. Acta Metall. 36, 3231 (1988).

[113] N.I. Medvedeva, Y.N. Gornostyrev, O.Y. Kontsevoi, A.J. Freeman. Acta Mater. 52, 675 (2004).

[114] J.R. Greer, J.Th.M. De Hosson. Prog. Mater. Sci. 56, 654 (2011).

[115] G. Abadias, S. Dub, R. Shmegera. Surf. Coat. Technol. 200, 6538 (2006).

[116] I. Salehinia, S. Shao, J. Wang, H. M. Zbib. JOM 66(10), 2078 (2014).

[117] S. B. Sinnott, E. C. Dickey. Mater. Sci. Eng. R Rep. 43, 1 (2003).

[118] W. D. Kingery, H. K. Bowen, D. R. Uhlmann. *Introduction to Ceramics*, 2nd edn. Wiley (1975).

[119] L. E. Toth, *Transition Metal Carbides and Nitrides*. Academic Press (1971).

[120] M. Oden, H. Ljungcrantz, L. Hultman. J. Mater. Res.12, 2134 (1997).

[121] A. M. Minor, E. A. Stach, J. W. Morris, I. Petrov. J. Elec. Mater. 32, 1023 (2003).

[122] J. D. Embury, J. P. Hirth. Acta Metall. Mater. 42, 2051 (1994).

[123] D. R. P. Singh, N. Chawla, G. Tang, Y.L. Shen. Acta Mater. 58, 6628 (2010).

[124] X. Deng, N. Chawla, K. K. Chawla, M. Koopman, J. P. Chu. Adv. Eng. Mater. 7, 1099 (2005).

[125] W. M. Mook, R. Raghavan, J. Baldwin, D. Frey, J. Michler, N. A. Mara, A. Misra. Mater. Res. Lett. 1, 102 (2013).

[126] D. Bhattacharyya, N. A. Mara, P. Dickerson, R.G. Hoagland, A. Misra. Philos. Mag. 90, 1711 (2010)

[127] S. A. Barnett, A. Madan. Scr. Mater. 50, 739 (2004).

[128] I. Salehinia, J. Wang, D. F. Bahr, H. M. Zbib. Int. J. Plast. 59, 119 (2014).

[129] A. Duck, N. Gamer, W. Gesatzke, M. Griepentrog, W. Osterle, M. Sahre, I. Urban. Surf. Coat. Technol. 142-144, 579 (2001).

[130] X. Deng, C. Cleveland, N. Chawla, T. Karcher, M. Koopman, K. K. Chawla. J. Mater. Eng. Perform. 14, 417 (2005).

[131] P. L. Sun, J.P. Chu, T.Y. Lin, Y.L. Shen, N. Chawla. Mater. Sci. Eng. A 527, 2985 (2010).

[132] G. Tang, Y.L. Shen, D. R. P. Singh, N. Chawla. Acta Mater. 58, 2033 (2010).

[133] D. Bhattacharyya, N. A. Mara, P. Dickerson, R.G. Hoagland, A. Misra. Acta Mater. 59, 3804 (2011).

[134] J. Wang, A. Misra. Curr. Opin. Solid State Mater. Sci. 18, 19 (2014).

[135] N. Li, H. Wang, A. Misra, J. Wang. Sci. Rep. 4, 6633 (2014).

IntechOpen